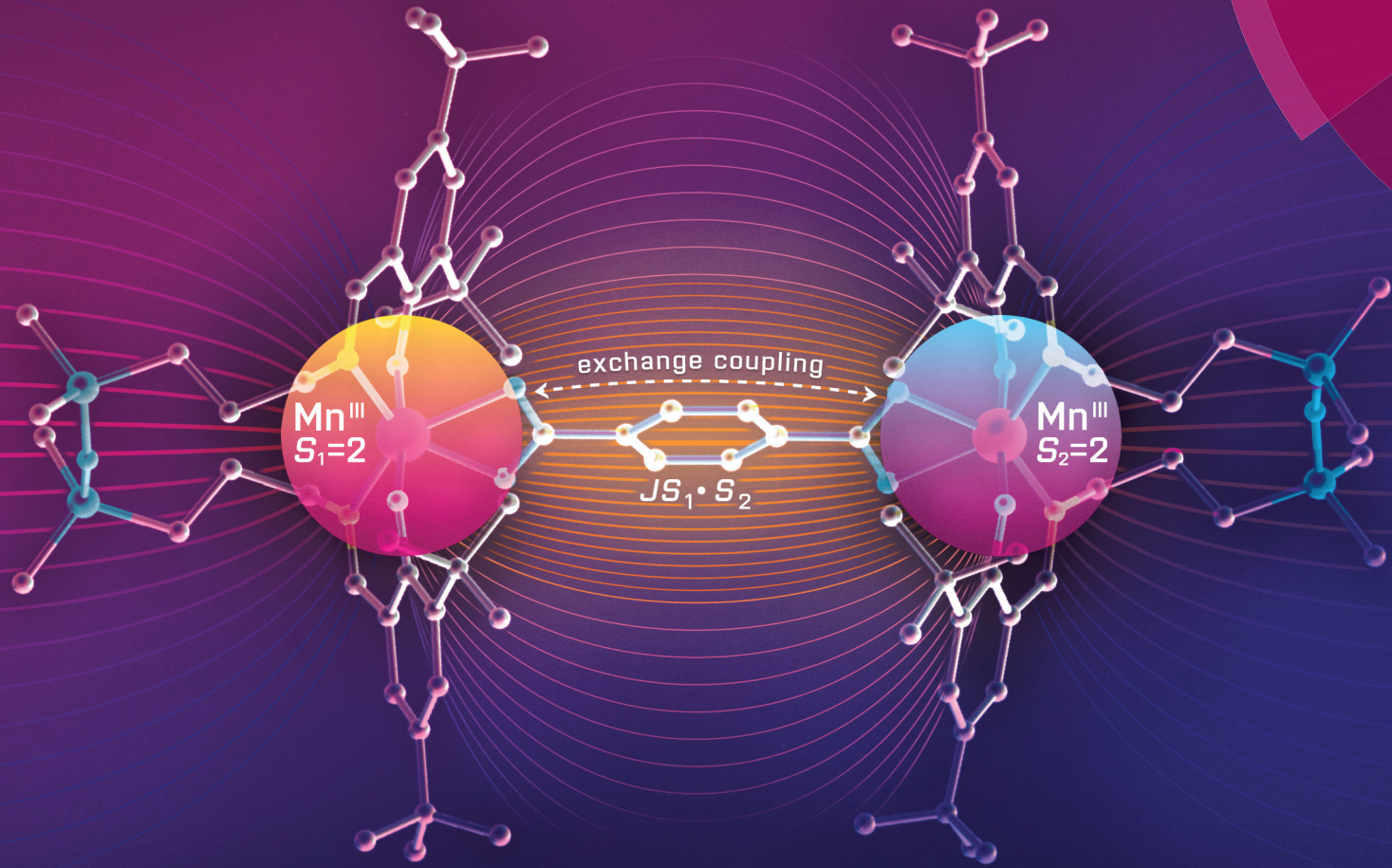


Dalton Transactions

An international journal of inorganic chemistry

rsc.li/dalton



Featuring the themed issue: Bioinspired Reactivity and Coordination Chemistry

ISSN 1477-9226



ROYAL SOCIETY
OF CHEMISTRY

Celebrating
IYPT 2019

PAPER

Joshua Telser, Vladimir B. Arion et al.

Dirinuclear manganese(III) complexes with bioinspired coordination and variable linkers showing weak exchange effects: a synthetic, structural, spectroscopic and computation study



Cite this: *Dalton Trans.*, 2019, **48**, 5909

Dinuclear manganese(III) complexes with bioinspired coordination and variable linkers showing weak exchange effects: a synthetic, structural, spectroscopic and computation study[†]

Sergiu Shova,^a Angelica Vlad,^a Maria Cazacu,^a J. Krzystek,^a Andrew Ozarowski,^a Michal Malček,^c Lukas Bucinsky,^c Peter Raptá,^c Joan Cano,^d Joshua Telser^a and Vladimir B. Arion^a^{*f}

Three dimanganese(III) complexes have been synthesised and fully characterised by standard spectroscopic methods and spectroelectrochemistry. Each Mn^{III} ion is chelated by a salen type ligand (H₂L), but there is variation in the bridging group: LMn(OOCCH=CHCOO)MnL, LMn(OOCC₆H₄COO)MnL, and LMn(OOCC₆H₄C₆H₄COO)MnL. X-ray diffraction revealed an axial compression of each six-coordinate high-spin d⁴ Mn^{III} ion, which is a Jahn-Teller-active ion. Temperature dependent magnetic susceptibility and variable temperature-variable field (VT VH) magnetisation measurements, as well as high-frequency and -field EPR (HFEPR) spectroscopy were used to accurately describe the magnetic properties of the complexes, not only the single-ion spin Hamiltonian parameters: g-values and zero-field splitting (ZFS) parameters D and E, but also the exchange interaction constant J between the two ions, which has been seldom determined for a di-Mn^{III} complex, particularly when there is more than a single bridging atom. Quantum chemical calculations reproduced well the electronic and geometric structure of these unusual complexes, and, in particular, their electronic absorption spectra along with the spin Hamiltonian and exchange parameters.

Received 20th November 2018,

Accepted 4th January 2019

DOI: 10.1039/c8dt04596h

rsc.li/dalton

Introduction

Dimanganese units have been discovered in a number of metalloenzymes, such as non-heme catalases,^{1–3} class 1b ribonucleotide reductases,^{4,5} Mn arginase,⁶ and bacterial thiosulfate oxidases.⁷ Therefore, the coordination chemistry of manganese has been in part developed by the desire to mimic the structure and spectroscopic properties of the active sites of these enzymes, and their catalytic activity. A large number of dimanganese complexes in various oxidation states with single fluorido,⁸ oxido/hydroxido/alkoxido,^{9–11} bis- μ -oxido/hydroxido/alkoxido,¹² μ _{1,3}-carboxylato¹³ and mixed oxido/hydroxido/alkoxido-carboxylato^{14–16} bridges and terminal carboxylato ligands¹⁷ have been synthesised and characterised over the years revealing structural, spectroscopic, or catalytic resemblance to the native enzymes. The progress in design and synthesis of low-molecular weight antioxidant catalysts as catalase-mimics has been recently reviewed.¹⁸ The Mn–Mn separation in these model compounds is usually around 3.0–3.7 Å, mimicking well the Mn–Mn distance in native enzymes. This di-Mn structure has been achieved by judicious ligand design. Dinucleating proligands,^{19,20} tridentate capping proligands such as tris(imidazole-2-yl)phosphine (TMIP),²¹ 1,4,7-triaza-

^aInorganic Polymers Department, “Petru Poni” Institute of Macromolecular Chemistry, Aleea Gr. Ghica Voda 41 A, Iasi 700487, Romania

^bNational High Magnetic Field Laboratory, Florida State University, Tallahassee, Florida 32310, USA

^cInstitute of Physical Chemistry and Chemical Physics, Slovak University of Technology in Bratislava, Radlinského 9, 81237 Bratislava, Slovak Republic

^dInstitut de Ciència Molecular, Universitat de València, Catedrático José Beltrán Martínez 2, 46980 Paterna, Spain

^eDepartment of Biological, Physical and Health Sciences, Roosevelt University, 430 S. Michigan Avenue, Chicago, Illinois 60605, USA. E-mail: jtelser@roosevelt.edu

^fInstitute of Inorganic Chemistry of the University of Vienna, Währinger Strasse 42, A1090 Vienna, Austria. E-mail: vladimir.arion@univie.ac.at

[†]Electronic supplementary information (ESI) available: Computational details and discussion of theoretically determined EPR properties; packing features of 1, 3 (Fig. S1) and 2 (Fig. S2), cyclic voltammograms of 1 and 2 (Fig. S3), HFEPR spectra of 1 and 2 (Fig. S4–S7), fragment of the experimental HFEPR spectrum of 1 and energy levels of a dimer with and without exchange interaction between Mn^{III} ions (Fig. S8), relative orientations of the experimental coordination sphere geometry of 1–3 and the calculated D tensor (Fig. S9); theoretical spin densities and electronic transitions of 1⁺ and 1²⁺ (Fig. S10); bond distances and angles 1–3 (Table S1), estimated values of the D and E/D ratio for 1–3 (Tables S2 and S3), calculated g-tensor components for 1–3 (Table S4), L-CASCI reference space used (Table S5). CCDC 1875357–1875359. For ESI and crystallographic data in CIF or other electronic format see DOI: 10.1039/c8dt04596h



cyclononane (tacn)²² and its derivatives, 1,4,7-trimethyl-1,4,7-triazacyclononane (Me_3tacn)^{8,23,24} and proline-derived tris-pyrrolidine-1,4,7-triazacyclononane,^{10,11} as well as hydrotris (pyrazol-1-yl)borate ($\text{HB}(\text{pz})_3$)^{22,25} have often been employed to facilitate the assembly of desired dimanganese cores by preventing polymeric chain formation.

Examples of dinuclear complexes with longer manganese-manganese distances are rare in the literature. Of note are the di- Mn^{III} complexes with two salen-type ligands separated by one or two xanthene spacer(s), in which the $\text{Mn}\cdots\text{Mn}$ separation was ~ 5.1 Å,²⁶ and with two salicaldehyde/diketonate-derived ligands in which the $\text{Mn}\cdots\text{Mn}$ separation was ~ 5.3 Å, and $\text{Mn}\cdots\text{Mn}$ exchange interactions were observed.^{27,28} Also notable are di- Mn^{II} expanded porphyrins with $\text{Mn}\cdots\text{Mn}$ distance of 5.4 Å,²⁹ and di- Mn^{II} complexes of bis(pentadentate) ligands derived from bis-tacn species with longer $\text{Mn}\cdots\text{Mn}$ distances (≥ 6.8 Å)³⁰ with no evidence of coupling between paramagnetic centres.

Recently, we reported on the synthesis of mononuclear 3d metal complexes with salen-type ligands bearing a disiloxane moiety (H_2L), which were shown to form a central 12-membered chelate cycle when binding to first row transition metal ions, *e.g.*, Cu^{II} , Fe^{III} , and Mn^{III} .^{31–34} In case of manganese, $\text{Mn}^{\text{III}}\text{L}(\text{OAc})$ and $\text{Mn}^{\text{III}}\text{L}(\text{NCS})$ were isolated and characterised by single crystal X-ray diffraction, routine spectroscopic methods (UV-vis, IR), spectroelectrochemistry, magnetochemistry, and high-frequency and -field EPR (HFEPR). We show herein that the 12-membered chelate cycle formed by coordination of this unusual salen-type ligand to manganese(III) precludes polymer formation and facilitates the assembly of di- Mn^{III} complexes by using as bridging ligands dicarboxylic acids. Dimanganese(III) complexes with fumarato, terephthalato, and/or *p*-diphenylcarboxylato bridging ligands were pre-

pared and fully characterised. These complexes are depicted in Fig. 1 and feature $\text{Mn}\cdots\text{Mn}$ distances ranging from 8.7 to 15.1 Å as controlled by the spacer group of the dicarboxylate. Previously reported dimanganese(III,IV) and dimanganese(II,III) systems have been investigated by HFEPR,^{35–37} and more importantly, so have dimanganese(III) complexes, such as a μ -oxido complex by Retegan *et al.*,¹⁰ a μ -fluorido complex by Pedersen *et al.*,⁸ and a system more relevant to those reported here, namely a dimanganese(III,III) complex without any bridging atoms, but with covalent connections between the two Mn^{III} ions *via* two *trans* four-bond π -conjugated O-C-C-C-O pathways.²⁸ A tetranuclear complex comprising a square grid of Mn^{III} ions linked by Schiff base ligands has also been studied by HFEPR,³⁸ but this complicated spin system is beyond the present study.

Interestingly, the HFEPR spectra observed here for the dinuclear complexes proved to be of better quality than those reported for the parent mononuclear complex $\text{Mn}^{\text{III}}\text{L}(\text{OAc})$. We note that the previous HFEPR studies of di- Mn^{III} complexes also exhibited very high quality spectra.^{8,10,28} These investigations taken together show that a reliable treatment of both the single-ion ZFS interaction and extraction of weak exchange interactions between paramagnetic Mn^{III} ($3d^4$) centres are possible.

Experimental

Materials

The complex $[\text{MnL}(\text{OAc})]\cdot0.15\text{H}_2\text{O}$, where H_2L is a tetradentate Schiff base with a tetramethyldisiloxane spacer, was prepared according to the procedure described previously.³¹ Fumaric acid (*trans*-HOOCCH=CHCOOH), benzene-1,4-dicarboxylic

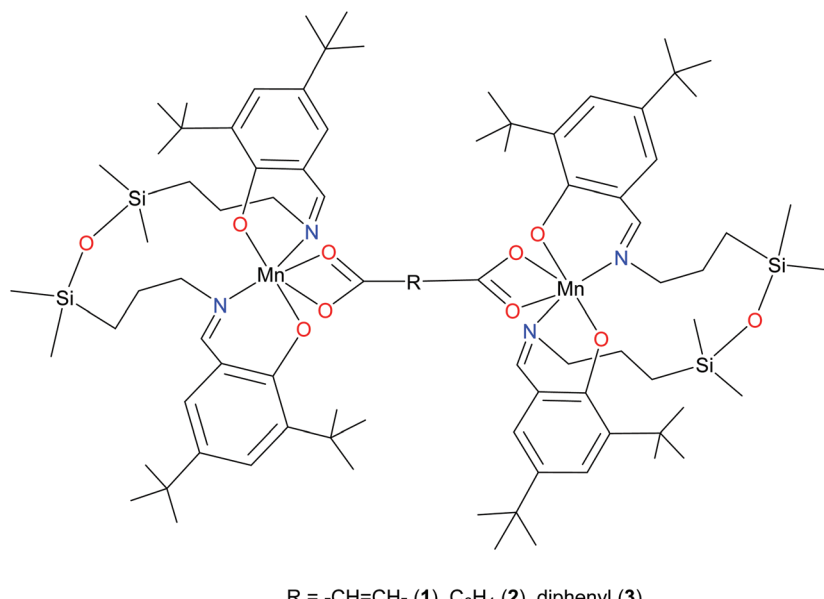


Fig. 1 Line drawing for complexes 1–3; bridging group as indicated.



acid (terephthalic acid, $C_6H_4\cdot1,4\cdot(CO_2H)_2$), and biphenyl-4,4'-dicarboxylic acid, 97% ($HO_2CC_6H_4C_6H_4CO_2H$) were all from Aldrich.

Synthesis of complexes

LMn(OOCCH=CHCOO)MnL·H₂O (1). A solution of MnL(OAc)·0.15H₂O (0.16 g, 0.2 mmol) in methylene chloride (20 ml) in a Schlenk tube was overlayed with a solution of fumaric acid (0.01 g, 0.1 mmol) in dimethylformamide (4 ml). The content was allowed to stand at room temperature. Brown sticks formed within one month and were separated by filtration, washed with diethyl ether and dried at room temperature. Yield: 0.11 g, 69.4%. Anal. Calcd (%) for $C_{84}H_{136}Mn_2N_4O_{11}Si_4$ (M_r 1645.26): C, 61.32, H, 8.64, N, 3.41. Found: C, 61.31, H, 8.40, N, 3.42. IR spectrum (KBr pellet), selected bands, ν_{max} (cm⁻¹): 3442w, 2956vs, 2868s, 1676vs, 1618vs, 1550s, 1440s, 1355m, 1298m, 1255vs, 1174m, 1066s, 977w, 921w, 885m, 840s, 785s, 746m, 698m, 634w, 565s, 509w, 468vw, 441w. X-ray diffraction quality crystals were grown from a mixture of CH₃OH:CH₂Cl₂ (~3:1). ESI-MS (positive ion mode): m/z 733.42 [Mn^{III}L]⁺.

LMn(OOCC₆H₄COO)MnL (2). A solution of MnL(OAc)·0.15H₂O (0.04 g, 0.05 mmol) in methylene chloride (4 ml) in a Schlenk tube was overlayed with a solution of terephthalic acid (0.003 g, 0.02 mmol) in dimethylformamide (4 ml). The content was allowed to stand at room temperature. Brown sticks formed within two weeks and were separated by filtration, washed with diethyl ether and dried at room temperature. Yield: 0.028 g, 68.7%. Anal. Calcd (%) for $C_{88}H_{136}Mn_2N_4O_{10}Si_4$ (M_r 1632.26): C, 64.75, H, 8.40, N, 3.43. Found: C, 64.74, H, 8.70, N, 3.45. IR spectrum (KBr pellet), selected bands, ν_{max} (cm⁻¹): 3888vs, 3874vs, 3668w, 3431w, 2956vs, 2912s, 2868m, 2395w, 2353w, 2326w, 1811w, 1791vw, 1753w, 1718w, 1678s, 1616vs, 1550s, 1506w, 1438s, 1390s, 1357m, 1253vs, 1205w, 1174m, 1070s, 923vw, 885m, 839vs, 806m, 783s, 750m, 702w, 636w, 565s, 509w, 439w, 403vw. X-ray diffraction quality crystals were grown from a mixture of CH₃OH:CH₂Cl₂ (~4:1). ESI-MS (positive ion mode): m/z 733.42 [Mn^{III}L]⁺.

LMn(OOCC₆H₄C₆H₄COO)MnL·H₂O (3). A solution of MnL(OAc)·0.15H₂O (0.02 g, 0.025 mmol) in methylene chloride (4 ml) in a Schlenk tube was overlayed with a solution of biphenyl-4,4'-dicarboxylic acid (0.003 g, 0.0125 mmol) in a mixture of dimethylformamide: methanol 1:1 (4 ml) at about 60 °C. The content was allowed to stand at room temperature. Brown sticks formed within one month and were separated by filtration, washed with diethyl ether and dried at room temperature. Yield: 0.02 g, 91.0%. Anal. Calcd (%) for $C_{94}H_{142}Mn_2N_4O_{11}Si_4$ (M_r 1726.37): C, 65.40, H, 8.29, N, 3.25. Found: C, 65.61, H, 8.19, N, 3.41. IR spectrum (KBr pellet), selected bands, ν_{max} (cm⁻¹): 3437m, 2956vs, 2910s, 2868s, 1676s, 1616vs, 1581m, 1541s, 1436s, 1396vs, 1355m, 1307m, 1253vs, 1174s, 1132w, 1064s, 972w, 921vw, 885m, 842vs, 777s, 694m, 636w, 567m, 509w, 439w. ESI-MS (positive ion mode): m/z 733.42 [Mn^{III}L]⁺.

Physical measurements. Infrared (IR) spectra of the compounds as pellets incorporated in dry KBr were recorded on a Bruker Vertex 70 FT-IR spectrometer, in transmission mode, in the range 400–4000 cm⁻¹ with a resolution of 2 cm⁻¹ and accumulation of 32 scans, at room temperature.

X-ray crystallography. The X-ray diffraction measurements were carried on a Bruker X8 APEXII CCD diffractometer using graphite monochromated MoK α radiation ($\lambda = 0.71073 \text{ \AA}$) at 100 K. The data were processed using SAINT software.³⁹ The structures were solved by direct methods using Olex2⁴⁰ and refined by full-matrix least-squares on F^2 with SHELXL-97⁴¹ using an anisotropic model for non-hydrogen atoms. All H atoms were introduced in idealised positions ($d_{CH} = 0.96 \text{ \AA}$) using the riding model with their isotropic displacement parameters fixed at 120% of their riding atom. The molecular plots were obtained using the Olex2 program. The crystallographic data and refinement details are quoted in Table 1, while bond lengths are summarised in Table S1, ESI.† CCDC – 1875359 for 1·6CH₂Cl₂, 1875358 for 2·4CH₂Cl₂ and 1875357† for 3·4.5H₂O contain the supplementary crystallographic data for this contribution.

Electrochemistry and spectroelectrochemistry. Cyclic voltammetric studies were performed using a glassy-carbon disc or platinum disc as working electrodes, Pt-wire as auxiliary electrode, and silver wire as pseudoreference electrode with a Heka PG310USB (Lambrecht, Germany) potentiostat. Ferrocene served as the internal potential standard and all potentials are quoted vs. the ferricinium/ferrocene (Fc⁺/Fc) couple. *In situ* spectroelectrochemical measurements were performed on Avantes, Model AvaSpec-2048x14-USB2 spectrometer under an argon atmosphere with the Pt-microstructured honeycomb working electrode, purchased from Pine Research Instrumentation (spectroelectrochemical cell kit AKSTCKIT3). In *ex situ* EPR spectroelectrochemical experiments at X-band at low temperatures, the initial dimer in MeCN/nBu₄NPF₆ was partially electrolysed in a coulometric cell using a large platinum-mesh working electrode at the maximum of the first oxidation peak. After an exhaustive electrolysis the solution was transferred into an EPR tube under argon at room temperature, and the EPR spectra were measured at 77 K, after freezing the sample in liquid nitrogen.

Magnetometry. Variable-temperature (2.0–300 K) dc magnetic susceptibility under an applied field of 0.25 ($T < 20 \text{ K}$) and 5.0 kG ($T \geq 20 \text{ K}$), and variable-field (0–5.0 T) magnetisation in the temperature range from 2 to 10 K were recorded with a Quantum Design SQUID magnetometer. The experimental magnetic susceptibility and magnetisation data of 1–3 were fitted with the VPMAG program⁴² using the spin Hamiltonian given next in the HFEPR section, but with an isotropic g value. The quality of the fit is defined by the F parameter that is the agreement factor defined as $\Sigma[P_{\text{exp}} - P_{\text{calcd}}]^2 / \Sigma[P_{\text{exp}}]^2$, with P being the physical property under study.

HFEPR. HFEPR spectra were recorded using a spectrometer that has been described previously,⁴³ with a difference of using a Virginia Diodes (Charlottesville, VA) source operating



Table 1 Crystallographic data, details of data collection and structure refinement parameters for **1**·6CH₂Cl₂, **2**·4CH₂Cl₂ and **3**·4.5H₂O

| Compound | 1·6CH ₂ Cl ₂ | 2·4CH ₂ Cl ₂ | 3·4.5H ₂ O |
|---|--|---|---|
| Empirical formula | C ₉₀ H ₁₄₆ Cl ₁₂ Mn ₂ N ₄ O ₁₀ Si ₄ | C ₉₂ H ₁₄₄ Cl ₈ Mn ₂ N ₄ O ₁₀ Si ₄ | C ₉₄ H ₁₅₁ Mn ₂ N ₄ O _{15.5} Si ₄ |
| <i>F</i> _w | 2091.75 | 1971.95 | 1807.43 |
| <i>T</i> [K] | 100 | 100 | 100 |
| Crystal system | Triclinic | Triclinic | Monoclinic |
| Space group | <i>P</i> 1 | <i>P</i> 1 | <i>P</i> 2 ₁ /c |
| <i>a</i> [Å] | 13.7007(7) | 11.8837(17) | 15.790(2) |
| <i>b</i> [Å] | 14.7166(7) | 12.7755(19) | 14.221(2) |
| <i>c</i> [Å] | 15.9617(8) | 18.564(3) | 23.958(3) |
| α [°] | 67.7592(16) | 73.414(5) | |
| β [°] | 66.1603(17) | 81.359(5) | |
| γ [°] | 79.2085(17) | 72.378(5) | |
| <i>V</i> [Å ³] | 2722.5(2) | 2568.1(6) | 5168.3(13) |
| ρ_{calcd} [g cm ⁻³] | 1.276 | 1.275 | 1.161 |
| <i>Z</i> | 1 | 2 | 4 |
| μ [mm ⁻¹] | 0.622 | 0.555 | 0.350 |
| Crystal size [mm] | 0.528 × 0.523 × 0.485 | 0.32 × 0.14 × 0.04 | 0.41 × 0.096 × 0.072 |
| 2 <i>θ</i> range | 4.88 to 60.22 | 4.62 to 50.06 | 4.56 to 50.06 |
| Reflections collected | 61 020 | 8962 | 64 669 |
| Independent reflections | 15 855 [<i>R</i> _{int} = 0.0461] | 8962 [<i>R</i> _{int} = 0.045] | 9090 [<i>R</i> _{int} = 0.0576] |
| Data/restraints/parameters | 15 855/6/605 | 8962/0/558 | 9090/3/567 |
| <i>R</i> ₁ ^a | 0.0539 | 0.0765 | 0.0779 |
| w <i>R</i> ₂ ^b | 0.1653 | 0.2270 | 0.2170 |
| GOF ^c | 1.040 | 1.061 | 1.030 |
| Largest diff. peak/hole/e Å ⁻³ | 1.04/−2.08 | 1.25/−1.15 | 1.88/−0.98 |

^a $R_1 = \sum |F_o| - |F_c| / |\sum F_o|$. ^b $wR_2 = \{\sum [w(F_o^2 - F_c^2)^2] / \sum [w(F_o^2)^2]\}^{1/2}$. ^c GOF = $\{\sum [w(F_o^2 - F_c^2)^2] / (n - p)\}^{1/2}$, where *n* is the number of reflections and *p* is the total number of parameters refined.

at 13 ± 1 GHz, amplified and multiplied by a cascade of frequency multipliers.

Multifrequency HFEPR data obtained for **1** and **2** were fitted using the following spin Hamiltonian:

$$H = \beta_e B g \hat{S} + D[\hat{S}_z^2 - S(S+1)/3] + E(\hat{S}_x^2 - \hat{S}_y^2) \quad (1)$$

in which the *g* tensor represents the Zeeman interaction, *D* and *E* are, respectively, the axial and rhombic ZFS components, and β_e is the electron Bohr magneton.

Computational methods. Magnetic properties of the compounds under study were evaluated with three different structural models to compare briefly the qualitative and/or quantitative robustness of the tools available to assess EPR parameters in the ORCA 4.0 programme:⁴⁴ (a) for Mn^{III}Ga^{III} dinuclear complexes; (b) for a mononuclear complex with a single Mn^{III} centre; and (c) a Mn^{III}Mn^{III} dinuclear complex in the large complete active space configuration interaction (L-CASCI) single centre approximation (see ESI† for the full computational details). These models are described in detail as follows:

(a) Theoretical calculations based on both an *ab initio* method, namely the Complete Active Space (CAS) multi-configurational method, as well as at the DFT level using the PBE functional,⁴⁵ on the full Mn^{III}Ga^{III} dinuclear complexes of **1**–**3** were performed for determining the Mn^{III} single-ion ZFS. These calculations were carried out using the TZVP basis set proposed by Ahlrichs^{46–48} and the auxiliary TZV/C Coulomb fitting basis sets.^{49–51} The second order contributions to ZFS were evaluated for the five quintet and 30 triplet excited states

generated from an active space with four electrons in five d orbitals. Furthermore, to estimate the dynamic electron correlation effects on ZFS parameters, mononuclear models built from a truncation of the original molecules were carried out by the CAS method and subsequent second-order N-electron valence state perturbation theory (NEVPT2).⁵²

(b) For the sake of comparison with the previous studies on [MnL(NCS)] and [MnL(OAc)],^{31,33} additional calculations have been performed using the BLYP functional⁵³ and 6-311G*⁵⁴ basis set using the CASSCF and Multi-Reference Configuration Interaction (MRCI) approaches. These calculations used the crystal structure geometries of **1**–**3** with the entire second Mn^{III}-containing moiety removed (refer to ESI† for further details). In addition, the effect of the solvent molecules present in the crystal structure has been studied for brevity at the BLYP/6-311G* level. The spin–spin interaction has been accounted *via* the MRCI⁵⁵ approach for the state-averaged quintet CASSCF(4,5) wave function.

(c) In addition, the multi-centre (*i.e.*, both Mn^{III}L moieties and the bridging ligand) CASSCF(8,10) ZFS parameters have been compared to CAS(8,10)-CI results (automatic auxiliary fitting basis set was used) for **1**–**3**. The L-CASCI approach has followed consistently the protocol as described in the literature.⁵⁶ The L-CASCI calculations accounted both for spin-orbit and spin–spin couplings (SOC and SSC, respectively).

For an additional comparison to spectroelectrochemistry studies, B3LYP⁵³/6-311G*⁵⁴ geometry optimisations of neutral (nonet), single (octet) and doubly (septet) charged species of **1**–**3** have been performed using the Gaussian09 software suite.⁵⁷ Subsequently, electronic transitions of all the B3LYP/6-



311G* optimised structures were evaluated using the TD-DFT method.⁵⁸ Herein, the 40, 60, and 80 lowest excited states were taken into account for the neutral, single and doubly charged species, respectively, to approach transition energies corresponding to $\lambda \geq 300$ nm. Spin densities were visualised using Molekel⁵⁹ software suite.

To extend further the computations used to assess the EPR parameters in the single-ion models, the possibility of a magnetic exchange interaction between the two Mn^{III} ions was studied at the DFT level of theory. These calculations were performed with the CAM-B3LYP hybrid functional using the Gaussian 09 package,⁵⁷ the quadratic convergence approach, and a guess function generated with the fragment tool of the same program.^{53,60} Triple- ζ and double- ζ all-electron basis sets proposed by Ahlrichs *et al.* were respectively employed for the Mn ions and the remaining atoms.^{47,48} The magnetic coupling states were obtained from the relative energies of the broken-symmetry (BS) singlet spin state from the high-spin state with parallel local spin moments.^{61–63} A polarisable continuum model (PCM) was introduced in the calculations with the parameters corresponding to acetonitrile.⁶⁴ To assure that the precision of the results was higher than the magnitude of the estimated J values, a triple- ζ basis set, adding an extra p polarisation function for all atoms, together with restricted conditions in the self-consistent convergence of the wave-function and in the evaluation of the bi-electronic integrals (very tight and ultrafine, respectively) were also employed.

Results and discussion

Synthesis

Complexes **1–3** were prepared by reaction of MnL(OAc) \cdot 0.15H₂O with fumaric acid, terephthalic acid, and biphenyl-4,4'-dicarboxylic acid in DCM/DMF or DCM/DMF/MeOH mixtures after long standing of the reaction mixture at room temperature. Recrystallisation of the crude products from DCM/MeOH 1 : 1 afforded single crystals of X-ray diffraction quality.

X-ray diffraction

The results of X-ray diffraction studies for **1–3** are shown in Fig. 2. All three dinuclear molecules exhibit similar molecular structure with each exhibiting its own crystallographically imposed inversion symmetry and show the presence of a half of dimeric molecule co-crystallised with 3CH₂Cl₂, 2CH₂Cl₂, and 2.25H₂O, respectively, in the asymmetric part of the unit cell. Each Mn atom is coordinated by N₂O₂ set of atoms originating from tetradeятate, doubly deprotonated Schiff base ligand and two oxygen atoms provided by the dicarboxylato anion in strongly distorted octahedral geometry. Further analysis of the coordination polyhedra indicates that the equatorial plane comprises N1 and N2 atoms of the tetradeятate ligand and two oxygen atoms of the dicarboxylato ion. The axial positions are occupied by the phenolate oxygen atoms. The axial bond lengths Mn–O1 and Mn–O2 are in the range of

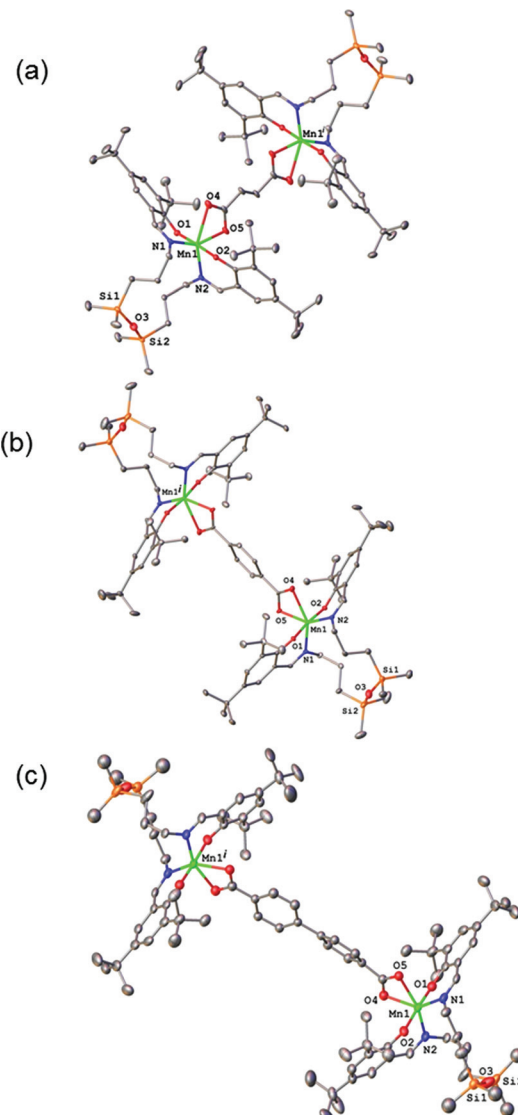


Fig. 2 X-ray molecular structure for (a) **1**, (b) **2**, and (c) **3** with selected atom labelling and thermal ellipsoids at 50% probability level. H-atoms are not shown. Symmetry codes (i): 2 - x, 2 - y, -z (for **1**); 2 - x, 1 - y, 1 - z (for **2**); 1 - x, 2 - y, -z (for **3**).

1.849(1)–1.870(1) Å. These are significantly shorter than the equatorial interatomic distances Mn–O and Mn–N in the range of 2.342(3)–2.077(3) Å, which indicates an axial compression in the distorted octahedron. The same coordination at the Mn site has been earlier reported for mononuclear compound [MnL(OAc)]³¹ where H₂L is *N,N*-bis(3,5-di-*tert*-butyl-2-hydroxybenzaldehyde) 1,3-bis(3-aminopropyl)tetramethylsiloxane. The average angle within the plane O4–Mn1–O5 is of 59.3(3)°, while N1–Mn1–N2 angle is of 120.5(3)° for **1–3**, respectively, reflects also the distortion of the octahedral geometry. The Mn–Mn distances in **1–3** are 8.736, 10.912 and 15.103 Å, respectively.

The analysis of the crystal structure packing revealed that all the compounds are associated in the crystal only through

the C-H $\cdots\pi$ interactions to form either supramolecular chains or ribbon-like aggregates. Thus, the crystal structures of **1** and **3** are built up from the parallel packing of one-dimensional chains, as shown in Fig. S1a and S1b (ESI \dagger), respectively. The crystal packing of **3** shows the presence of the supramolecular ribbons (Fig. S2, ESI \dagger).

Electrochemistry and spectroelectrochemistry

The anodic oxidation of complexes **1**–**3** is irreversible as shown in Fig. 3 and is similar to the monomeric MnL(OAc) analogue.³¹ Only a small, broad, cathodic peak can be observed upon the voltammetric scan reversal, even at low scan rates, indicating subsequent irreversible chemical reactions of the oxidised dimeric complexes.

A small additional peak is seen behind the first one for **1** and **3** which height varies from scan to scan indicating the follow up reactions of the oxidised state (see also Fig. S3a, ESI \dagger). No reduction processes were observed in cathodic region (see Fig. S3b, ESI \dagger) as also noted for MnL(OAc). After electrolysis of **1**–**3** in the region of the first irreversible oxidation peak, no X-band EPR signal was observed even at 77 K further indicating a low stability of the oxidised form of **1**–**3**. Although a negative EPR result at 77 K is not proof of the inability to electrochemically generate Mn^{IV} species in solution, we note that a variety of *bona fide* Mn^{IV} coordination complexes exhibit EPR spectra (even in some cases as magnetically undiluted solids) at temperatures as high as ambient.^{65–67} However, there are small differences in the voltammetric responses found for **1**–**3**. The highest oxidation potential was found for **2** with only one oxidation peak demonstrating the (electro)chemical equivalence of the two Mn^{III} sites and the lack of measurable interaction between them, consistent with the magnetometry and HFEPR. For **3** the lowest oxidation

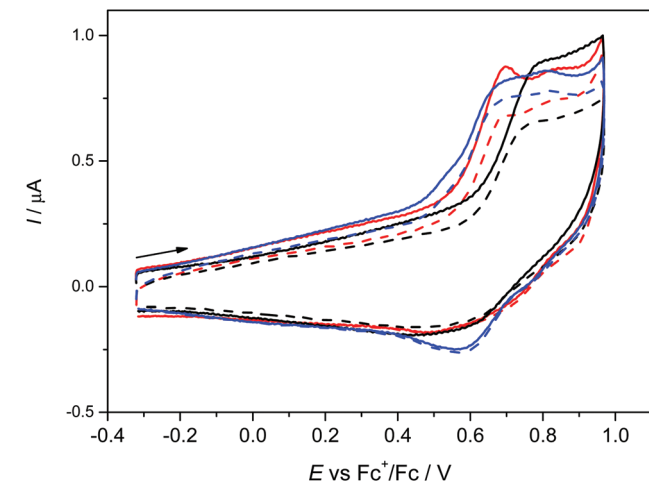


Fig. 3 Cyclic voltammograms of 0.15 mM **1** (red traces), **2** (black traces) and **3** (blue traces) in $n\text{Bu}_4\text{NPF}_6/\text{CH}_2\text{Cl}_2$ (GC-disc working electrode, scan rate 100 mV s $^{-1}$, solid line – the first voltammetric scan, dashed line – the second scan).

potential was found with two overlapping oxidation peaks again indicating two almost equal Mn^{III} redox centres.

Analogously to the voltammetric studies, the optical spectra of **1**–**3** are very similar with low-intensity bands at 480, 670 and at around 730 nm (Fig. 4a).

Taking into account our previous works^{31,33} on mono-nuclear Mn^{III}L(OAc) and Mn^{III}L(NCS), the first low-energy electronic transition at 730 nm can be assigned to LMCT from phenolate moieties to manganese(III) with a strong charge transfer from phenolic moieties to the central Mn atom and the corresponding coordination polyhedron. The *in situ* UV-vis-NIR spectroelectrochemical experiments confirmed irreversible changes upon anodic oxidation of **1**–**3** in the region of the first oxidation peak (from +0.2 V to +0.9 V vs. Fc $^+$ /Fc) as illustrated for **2** in Fig. 4b. A new optical band at 360 nm emerged upon oxidation and simultaneously the maximum of the low-energy band shifted from 720 nm to 675 nm (see inset

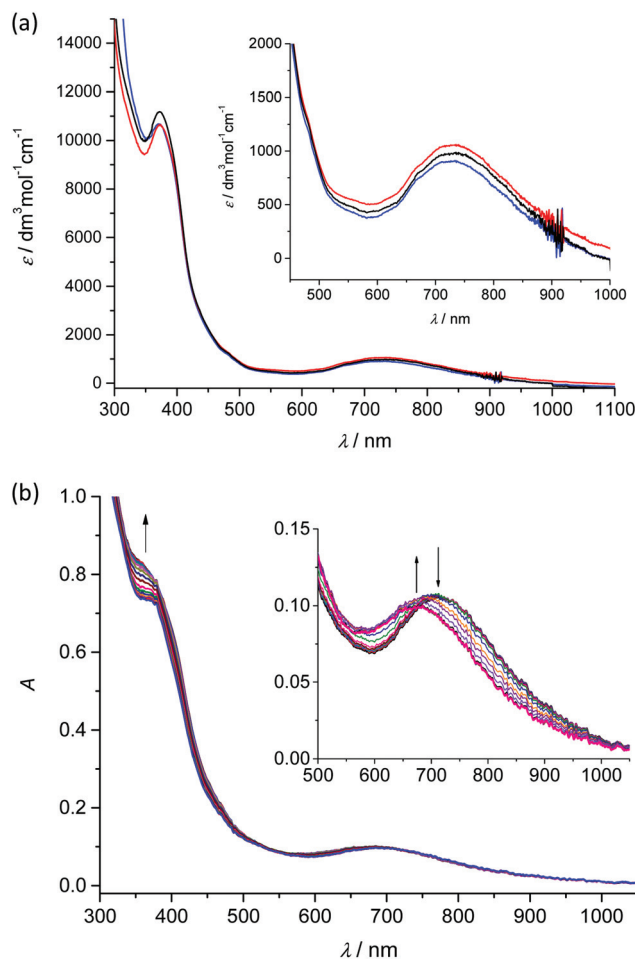


Fig. 4 (a) UV-vis-NIR spectra of **1** (red traces), **2** (black traces) and **3** (blue traces) in CH_2Cl_2 . (b) *In situ* optical spectroelectrochemistry for **2** in $n\text{Bu}_4\text{NPF}_6/\text{CH}_2\text{Cl}_2$ (scan rate 10 mV s $^{-1}$, Pt-microstructured honeycomb working electrode): UV-vis-NIR spectra recorded simultaneously upon the *in situ* oxidation in the region of the first anodic peak (from +0.2 V to +0.9 V vs. Fc $^+$ /Fc). Inset in (b): expansions of the vis-NIR bands.



in Fig. 4b). However in contrast to the recently studied $\text{Mn}^{\text{III}}\text{L}(\text{NCS})$ complex,³⁴ upon scan reversal the products that are formed upon oxidation are not reoxidised and no recovery of the initial optical bands upon the voltammetric reverse scan occurred, confirming the low stability of Mn^{IV} state as also reported for the $\text{Mn}^{\text{III}}\text{L}(\text{OAc})$.³¹

Magnetometry

The direct current (dc) magnetic properties of **1–3** were measured per dinuclear complex and are presented in the form of plots of $\chi_M T$ vs. T and M vs. H/T , as shown in Fig. 5. The $\chi_M T$ values at room temperature (6.02, 6.20, and 6.07 $\text{cm}^3 \text{K mol}^{-1}$ for **1–3**, respectively) are close to that expected for two isolated $S = 2$ centres ($6.0 \text{ cm}^3 \text{K mol}^{-1}$, $g = 2.0$). When cooling down, the $\chi_M T$ value remains constant until 40 K and then decreases abruptly to reach a value at 2 K of 4.29, 4.02, and 3.99 $\text{cm}^3 \text{K mol}^{-1}$ for **1–3**, respectively. The isothermal magnetisation curves do not superimpose, and the magnetisation values at 5 T and 2 K (6.62, 6.54, and 6.49 $N\beta$ for **1–3**) are below the saturation limit of $8N\beta$ for two $S = 2$ with $g = 2$. This behaviour could be due to the presence either of magnetic exchange coupling⁶⁸ or single-ion zero-field splitting (ZFS). The distance between the two Mn^{III} ions, is quite large (8.736 Å, 10.912 Å, and 15.102 Å for **1**, **2**, and **3**, respectively), so the electron dipole–dipole coupling would be very small (-0.008 cm^{-1} for **1** and -0.004 cm^{-1} for **2**, see below). Moreover, Mn^{III} in such a coordination geometry has been amply demonstrated to exhibit ZFS.^{27,69} Consequently, only ZFS would be responsible for the drop of $\chi_M T$ at low temperature. Evidence for weak exchange coupling between the Mn–Mn ions will be described below, along with computational studies probing this phenomenon. The best-fit obtained parameters are: $g = 2.004$, $D = +3.07 \text{ cm}^{-1}$, $E/D = 0.000$ ($F = 7.7 \times 10^{-5}$) for **1**; $g = 2.033$, $D = +3.45 \text{ cm}^{-1}$, $E/D = 0.009$ ($F = 4.4 \times 10^{-6}$) for **2**; and $g = 2.019$, $D = +3.63 \text{ cm}^{-1}$, $E/D = 0.002$ ($F = 6.6 \times 10^{-5}$) for **3**. The low values of the E/D ratio are not in agreement with those obtained by HFEPR spectroscopy, but this is caused by the poor sensitivity of dc susceptibility to this parameter. More importantly, the positive D values agree with the axial compression observed in the octahedral coordination sphere.^{69a,f,70,71}

HFEPR

Complex **1** when measured as is, *i.e.* unconstrained, produced strong spectra that showed symptoms of field-induced torquing. We did not try to interpret them, but proceeded to experiments on an *n*-eicosane pellet. Typical low-temperature spectra of **1** as a pellet are shown in Fig. 6 (top part), accompanied by simulations assuming a perfect powder distribution of the crystallites in space. Spectra at two lower frequencies are shown as Fig. S4 and S5, ESI.† The agreement between the simulations and experiments can be described as very good, assuming a spin state $S = 2$ characteristic for an individual (not coupled) Mn^{III} ion and under the condition of $D > 0$.

Complex **2** was visibly more crystalline than **1**. This required extensive grinding prior to pressing it into a pellet. A typical low-temperature pellet spectrum is shown in Fig. 6 (bottom),

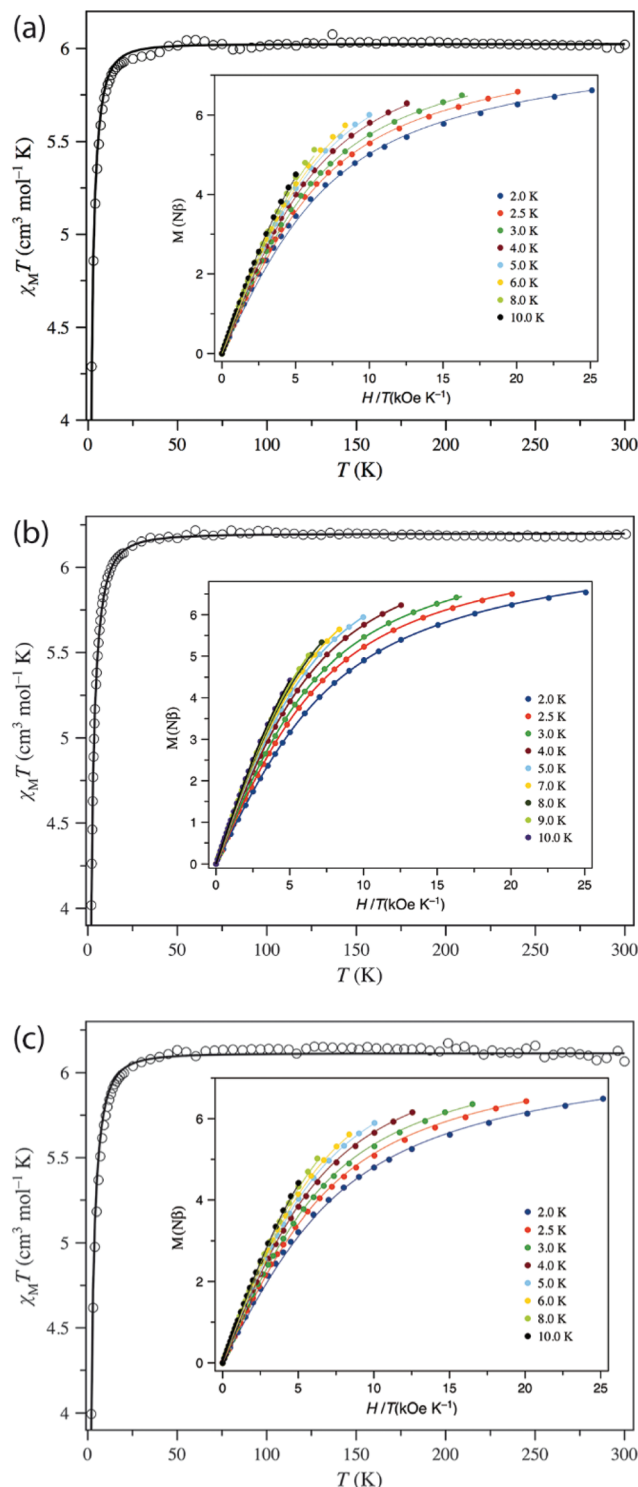


Fig. 5 Plots of $\chi_M T$ vs. T in the range 2–300 K in a 0.025 ($T < 20 \text{ K}$) and 0.5 T ($T \geq 20 \text{ K}$) applied field and M vs. H/T (inset) for (a) **1**, (b) **2**, and (c) **3** in the 2–10 K temperature range. The solid lines are the best-fit curves, with the fit parameters given in Table 2.

accompanied by simulations assuming a perfect powder distribution of the crystallites in space. Additional spectra at two different frequencies are shown in Fig. S6 and S7, ESI.† The



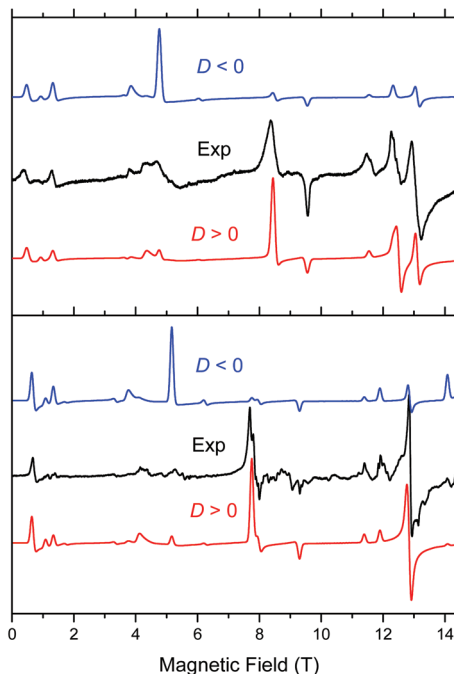


Fig. 6 Low-temperature HFEPR spectra of **1** at 422.4 GHz and 15 K (top) and **2** and 406.4 GHz and 10 K (bottom, both represented as black traces) accompanied by simulations using $S = 2$ spin Hamiltonian parameters as in Table 2. Blue traces: simulations using negative D ; red traces: positive D .

spectral quality was somewhat lower than that for **1** because of the sample crystallinity, yet the agreement between the simulations and experiments can be also described as very good, assuming again an $S = 2$ spin state, and under the condition of $D > 0$. The spin Hamiltonian parameters are similar but not identical to those of **1**.

Both complexes produced HFEPR spectra at any temperature between liquid helium and ambient. Fig. 7 shows their room-temperature spectra, again with simulations. In complex **1**, the axial ZFS parameter D is almost unchanged between liquid helium and room temperature (Table 2), but $|E|$ strongly decreases, the ZFS tensor becoming almost axial. In **2**, both parameters slightly decrease from low to high temperature.

A careful inspection of certain turning points in the low- T HFEPR spectra of both **1** and **2** reveals spectral regions at any frequency >200 GHz that show a fine but not quite regular structure with a period of *ca.* 60–80 mT (Fig. 8). The average value of 70 mT corresponds to 0.065 cm^{-1} , which is very small on the HFEPR scale as it corresponds to $\sim 2\text{ GHz}$ ($\sim 1\%$ of the frequency used in Fig. 8, right), but is still well within spectral resolution present. Yet, this energy is one order of magnitude more than that from ^{55}Mn hyperfine coupling, which could (potentially) be expected to appear in the spectra.⁷⁰ We postpone a discussion of this observation noting qualitatively that this could be a symptom of a very weak ($<0.1\text{ cm}^{-1}$) exchange taking place between the two Mn^{III} ions in the dimer.

The low- T spin Hamiltonian parameters used in the simulations shown in Fig. 6 were not deduced from the single-fre-

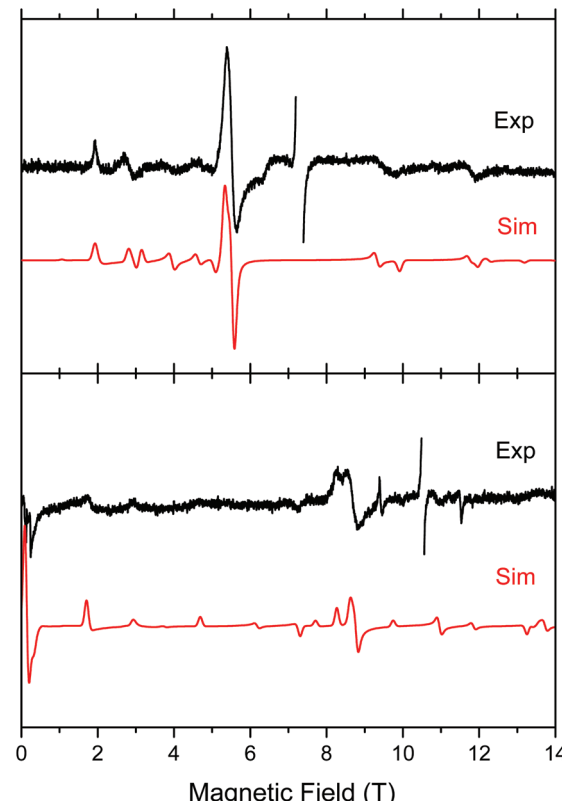


Fig. 7 Room-temperature HFEPR spectra of **2** at 203.2 GHz and 280 K (top) and **2** at 295.2 GHz and 277 K (bottom, black traces) accompanied by simulations using spin Hamiltonian parameters as in Table 2. At these temperatures, there is no difference between negative and positive D reflected in the spectra, thus the simulation (red trace) used positive D only. The Mn^{II} impurity resonances at $g = 2.00$ were left out of the experimental spectra and are not simulated.

quency spectra, but from the 2-D maps of turning points as a function of frequency/energy according to the principle of tuneable-frequency EPR.⁷² These maps are shown in Fig. 9. The parameters are listed in Table 2. The room temperature parameters, to the contrary, were obtained from single-frequency spectra only and because of the poor S/N are estimates only.

To explore the effect of the interactions between the Mn^{III} ions, the spin Hamiltonian in eqn (1) must be replaced by eqn (2) which operates within the space of 25 microstates in a system of two ions with $S_1 = S_2 = 2$:

$$\begin{aligned}
 H = & \mu_B \mathbf{B} \{g_1\} \hat{\mathbf{S}}_1 + \mu_B \mathbf{B} \{g_2\} \hat{\mathbf{S}}_2 \\
 & + D \left\{ \hat{S}_{1z}^2 - \frac{1}{3} S(S+1) \right\} + E \left\{ \hat{S}_{1x}^2 - \hat{S}_{1y}^2 \right\} \\
 & + D \left\{ \hat{S}_{2z}^2 - \frac{1}{3} S(S+1) \right\} + E \left\{ \hat{S}_{2x}^2 - \hat{S}_{2y}^2 \right\} \\
 & + J \hat{\mathbf{S}}_1 \hat{\mathbf{S}}_2 + D_{12} \left\{ \hat{S}_{1z} \hat{S}_{2z} - \frac{1}{3} \hat{\mathbf{S}}_1 \hat{\mathbf{S}}_2 \right\}
 \end{aligned} \quad (2)$$

where the terms with J and D_{12} describe the isotropic and anisotropic parts of the exchange interaction, respectively.^{68,73}

Table 2 Spin $S = 2$ Hamiltonian parameters for complexes **1** and **2** obtained from HFEPR at low, and high temperature limits and from VT dc magnetic susceptibility (magn.)

| Complex | T (K) | D (cm^{-1}) | $ E $ (cm^{-1}) | $ E/D $ | g_x | g_y | g_z^a |
|-------------------------------|------------------|--------------------------|----------------------------|---------|----------|----------|----------|
| 1 | 15 | +3.246(5) | 0.425(3) | 0.13 | 1.991(4) | 2.003(4) | 2.015(5) |
| 1 | 280 ^c | 3.27 | 0.10 | 0.03 | 1.98 | 1.98 | 2.00 |
| 1 (magn.) | NA | +3.07 | 0 | 0.000 | — | — | 2.004 |
| 2 | 10 | +2.997(3) | 0.530(1) | 0.18 | 1.991(5) | 1.991(5) | 1.991(5) |
| 2 | 277 ^c | 2.88 | 0.44 | 0.15 | 1.99 | 1.99 | 1.99 |
| 2 (magn.) | NA | +3.45 | 0.03 | 0.009 | — | — | 2.033 |
| 3 ^b (magn.) | NA | +3.63 | 0.007 | 0.002 | — | — | 2.019 |

^aThe magnetic fits used an isotropic g value which is given only in this column. ^bCompound **3** was investigated only by magnetometry due to material limitations. ^cThe room temperature HFEPR parameters are of lower precision (not specified) and are provided primarily to demonstrate that the electronic structures of **1** and **2** remain essentially unchanged over a wide temperature range.

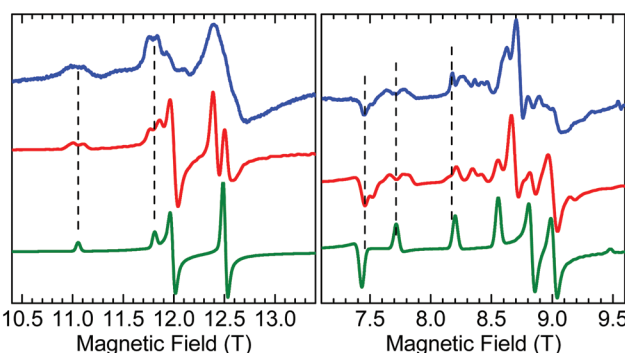


Fig. 8 Fragments of HFEPR spectra of **1** at 406.4 GHz and 10 K (left) and **2** at 203.2 GHz and 10 K (right). Blue: Experimental. Red: Calculated using spin Hamiltonian 2 (dimer model, eqn (2)). Green: Calculated using spin Hamiltonian 1 (monomer model, eqn (1)). The indicated splittings appear also in other regions of the spectra, and at different frequencies.

Since the molecules are centrosymmetric, the zero-field splitting tensors of the two Mn^{III} ions have the same components, $D_1 = D_2 \equiv D$ (thus D, E are as in eqn (1)) and are coaxial as well.⁷⁴ In the present case, D_{12} is most likely due only to the magnetic dipole–dipole interaction, which depends on the crystallographically-determined inter-ion distance R and can be estimated from:

$$D_{12} = -\frac{3g^2\mu_B^2}{R^3} \quad (3)$$

The largest component of the dipolar tensor is along the Mn–Mn direction which is almost perpendicular to the expected direction of the largest component of the ZFS tensor on each Mn^{III} ion, which is along the $\text{O}_{\text{(phenolato)}}\text{–Mn–O}_{\text{(phenolato)}}$ axis (*i.e.*, the axial compression axis; see discussion below and Fig. S9, ESI†). Eqn (3) results in D_{12} values of -0.008 cm^{-1} for **1** and -0.004 cm^{-1} for **2**. These magnitudes should be treated as an upper estimation as delocalisation effects of the Mn^{III} spins are not taken into account, but are even so much too small to account for the observed splitting of at least $\sim 60 \text{ mT}$. Nevertheless, for completeness, the EPR simulations for both **1** and **2** included these D_{12} values.

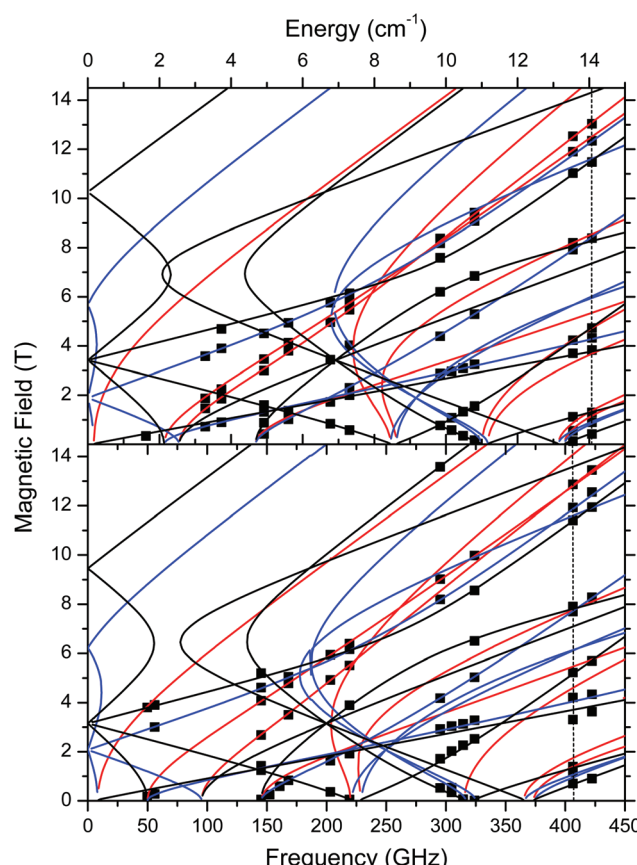


Fig. 9 Field vs. frequency/energy map of turning points in complexes **1** (top) and **2** (bottom) at 10–15 K. Squares are experimental points; curves were simulated using spin Hamiltonian parameters as in Table 2. Red curves: turning points with magnetic field B_0 parallel to the x -axis of the ZFS tensor; blue: $B_0 \parallel y$; black: $B_0 \parallel z$. The two dashed vertical lines indicate the frequencies at which spectra shown in Fig. 6 were recorded.

In contrast, for systems with single atom bridges, such as μ -oxido^{10,11} or -fluorido,⁸ the crystallographically-determined distances of $\sim 3.16 \text{ \AA}$ and 4.10 \AA , would give a maximum direct dipole–dipole coupling some 20 times larger: -0.16 cm^{-1} and -0.075 cm^{-1} , respectively. Even in the phenolato/diketonato-linked complex, the Mn–Mn distance of 5.26 \AA would give $D_{12} \approx -0.036 \text{ cm}^{-1}$.



However, in each of these three complexes previously studied by HFEPR, a direct covalent pathway between the Mn^{III} ions leads to an isotropic exchange interaction (eqn (2)) that overwhelms the dipolar effect. Use of the JS_1S_2 formalism (as opposed to $-2J$ or other variants) yields J (in cm^{-1}) = -2.3 , $+33.0(2)$, and $+1.70$, as respectively reported for each.^{8,10,11,28} The linear $\text{Mn}^{\text{III}}(\mu\text{-F})\text{-Mn}^{\text{III}}$ leads to a strong antiferromagnetic “bonding-like” interaction, but in the other complexes the anti- or ferromagnetic nature of the exchange coupling is not obvious. As explored by Retegan *et al.*,¹⁰ and others^{24,75} for di- Mn^{III} , by Morsing *et al.* for di- Cr^{III} ,⁷⁶ and by Weihe and Güdel for di- Fe^{III} ,⁷⁷ the specific geometry of the $\text{M}(\mu\text{-O[X]})\text{-M}$ moiety ($\text{X} = \text{none, H, R}$) has a profound effect on the exchange coupling parameter.

In our systems, wherein the Mn–Mn distances are much greater and the covalent pathways more convoluted, simulations nevertheless show that the isotropic exchange interaction is indeed responsible for the observed spectral effects. The J (and D_{12} , if it were larger) terms split the energy levels of a monomer which results in splitting of the single-ion resonances calculated using eqn (1) each into several components (Fig. 10 and S8, ESI†). Since powder spectra are superpositions of a very large number of single-crystal spectra, these splittings are mostly blurred and are recognisable only in certain magnetic field ranges allowing only a rough estimation of J .

Nevertheless, one can see that in **1**, an isotropic exchange term with $J = -0.025 \text{ cm}^{-1}$ (ferromagnetic), which is some 100 times smaller than D , is sufficient to split a “z” transition in **1**, which in a monomer occurs at 11.16 T, so that the outermost components are 180 mT apart (Fig. 6, 8, 10, and S8, ESI†). Spectra of **2** appear to simulate better with positive J of $+0.035 \text{ cm}^{-1}$. It is clear that exchange interactions of such small energy cannot be detected by magnetic measurements, nor would they affect the electrochemistry. The J magnitudes above must be treated as estimations, but single-crystal EPR experiments may provide accurate J values. Interestingly, some of us have recently observed similar effects in HFEPR of very different systems.⁷⁸ It should also be noted that NMR can be

used to probe exchange couplings as shown by the linear correlation between μ -acetato methyl proton chemical shifts and J values that was established for a series of dimanganese(III) complexes containing $\{\text{Mn}_2\text{O}(\mu\text{-O}_2\text{CCH}_3)_2\}^{2+}$ cores.²²

Computational studies

The magnetic EPR parameters assessment has been performed in three different approaches (a)–(c) (see Computational methods section, ESI†) to test the quality and robustness of the different models, options and choice of approximation, *i.e.* choice of method (*ab initio* vs. DFT/functional), basis set, integral treatment and single vs. multicentre approach. The results from the different *ab initio* methods are collected in Table 3.

The obtained results lead to a positive D value (Table 3) which is consistent with the axial (tetragonal) compression observed experimentally in the three complexes (Table 2), but with a significant rhombic distortion, in agreement with HFEPR spectroscopy. This similar axial distortion in **1**–**3** leads to close D values. However, the trend in the SOC CAS results is also corroborated by DFT calculations (Tables S2 and S3, ESI†), although this method underestimates the D values in manganese(III) complexes.^{32,34,55b} Generally, the SOC CAS results lead to an increase of D parameter with the size of the bridging ligand (see Table 3), which correlates well with the susceptibility fit in Table 2. On the contrary, the inclusion of SSC *via* MRCI reverses this trend in the single centre calculations of model (b) (see Table 3), which is in accordance with HFEPR (see Table 2) for **1** and **2**. HFEPR of powders or solutions does not provide the orientation of the ZFS. However, this can be calculated, and in Fig. S9 (ESI†) are displayed the orientations of the principal axes of the D tensors of **1**–**3** in the molecular coordinate system obtained in model (a). As expected, the principal z -axis (“hard” axis) points at the oxygen atoms of the coordinated phenolato groups, *i.e.*, along the axis of compression. Lastly, the g -tensors for **1**–**3** calculated from the NEVPT2 method and using an effective Hamiltonian for the spin-orbit coupling (Table S4, ESI†) agree moderately well with those obtained by HFEPR spectroscopy, with the calcu-

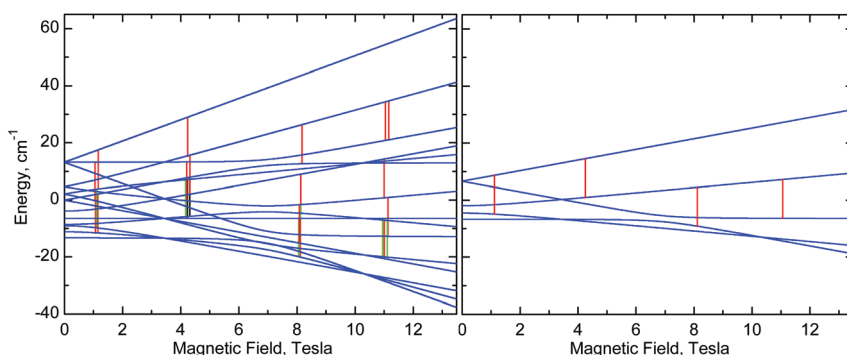


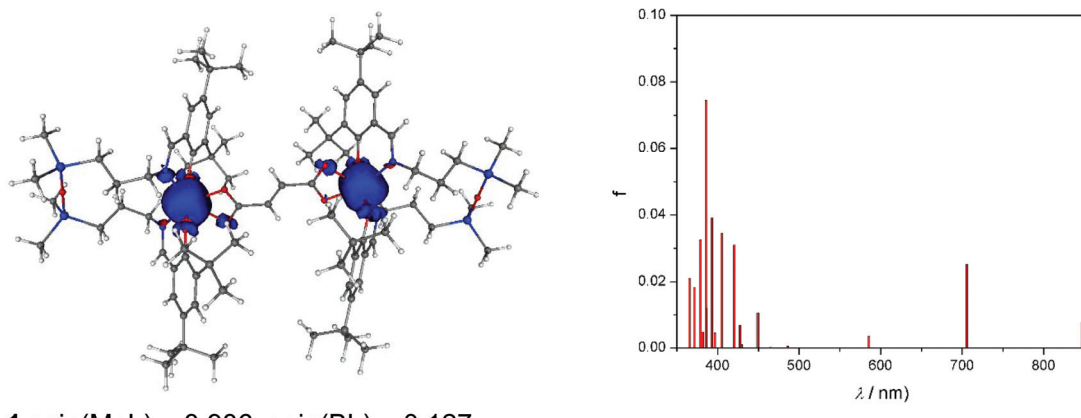
Fig. 10 Right: Energy levels of a monomer, calculated at the “z” orientation, using eqn (1) with parameters of **1** (Table 2). Left: Energy levels of a dimer, calculated using eqn (2) with the same single-ion g , D and E parameters of **1** and with $J = -0.025 \text{ cm}^{-1}$. The vertical lines represent EPR transitions expected at $\nu = 406.4 \text{ GHz}$. Only transitions with substantial probability are drawn. Colours are used to distinguish very close transitions. See also Fig. S8, ESI†



Table 3 Calculated values of the D (in cm^{-1}) and E/D ratio (in parentheses) for **1–3**

| Complex | Method | CAS ^a | NEVPT2 ^a | CAS (SOC) ^b | L-CASCI (SOC) ^b | MRCI (SOC + SSC) ^b | L-CASCI (SOC) ^c | L-CASCI (SOC + SSC) ^c |
|----------|--------|------------------|---------------------|------------------------|----------------------------|-------------------------------|----------------------------|----------------------------------|
| 1 | | +3.44 (0.234) | +3.57 (0.227) | +2.94 (0.228) | +2.93 (0.227) | +3.64 (0.136) | +2.62 (0.224) | +3.47 (0.234) |
| 2 | | +3.55 (0.159) | +3.64 (0.154) | +3.03 (0.154) | +3.03 (0.155) | +3.52 (0.159) | +2.71 (0.151) | +3.58 (0.163) |
| 3 | | +3.67 (0.151) | +3.87 (0.147) | +3.14 (0.133) | +3.14 (0.132) | +3.41 (0.232) | +2.81 (0.129) | +3.69 (0.137) |

^a Calculated for single-centre geometries from a second order perturbative spin-orbit coupling Hamiltonian applied to the CAS MnGa model and NEVPT2 wavefunctions of the single Mn centre (using TZVP basis set) of model (a). ^b Calculated for single-centre geometries (using 6-311G* basis set) of model (b). ^c Calculated for two-centre (using 6-311G* basis set and the autoaux density fitting basis set) using model (c).



1 $\text{spin}(\text{MnL}) = 3.936$, $\text{spin}(\text{BL}) = 0.127$

Fig. 11 Visualisation of spin density, including spin density populations on the Mn – tetradeinate Schiff base moiety MnL and on the bridging ligand BL (left) and calculated TD-DFT transitions (right) of the neutral **1** (nonet) species. The values of spin densities are in a.u. The isovalue was set to ± 0.005 a.u.

lated values being slightly below 2.0 which agrees with the high temperature HFEPR fit in Table 2, and is expected from classical theory for a less than half-filled d^n system.

As can be seen from Fig. 11, spin density is localised almost exclusively in the vicinity of the two Mn^{III} ions in the case of the neutral complex **1**. Upon oxidation to **1**⁺, part of the spin (about 0.5e) vanishes from these ions (Fig. S10a†). Finally, the doubly charged species, **1**²⁺ (septet), has the spin population decreased by one, hence both centres are oxidised to Mn^{IV} (Fig. S10b†). The calculated TD-DFT transitions (Fig. 11a) of **1** are in qualitative agreement with the experimental UV-vis spectra (Fig. 4). Comparison of singly and doubly oxidised species with the measured difference spectra are not useful due to irreversible chemical changes of **1–3** upon oxidation.

Finally, CAM-B3LYP DFT calculations on **1–3** showed that the intramolecular magnetic coupling in **1** is ferromagnetic (*i.e.*, J exchange coupling constant is negative: $H = JS_1S_2$) and weak, $J = -0.007 \text{ cm}^{-1}$, while in **2** and **3** it is antiferromagnetic with J of 0.004 and 0.022 cm^{-1} , respectively. The magnetic communication in an extended pathway can occur only through a π -pathway. A loss of its planarity causes a notable decrease in the aromaticity and the magnetic coupling. In **1–3**, the privation of this planarity comes mainly from a twist between the carboxylate groups and the vinyl (in **1**: 11.3° twist)

or phenyl rings (**2**: 26.2° and **3**: 17.4 – 20.0°), and between phenyl rings in **3** ($\approx 38^\circ$). Neither these structural distortions nor electronic effects such as accidental orthogonality of magnetic orbitals can explain the trend found for the J constants for **1–3**. Hence, speculation as to the structural/electronic basis for the opposite type of exchange coupling in **1** *versus* **2** and **3** is unwarranted given the very small magnitude of these interactions and the challenges of understanding exchange interactions even in singly bridged systems.^{10,24,68,75,79} Nevertheless, the DFT results for **1** and **2** are in qualitative agreement with the EPR data.

Conclusions

By using the ability of manganese(III) to form a six-coordinate complex with a salen type ligand bearing a disiloxane unit and an acetate as bidentate co-ligand described previously, three dimanganese(III) complexes have been synthesised and characterised by standard analytical and spectroscopic techniques, X-ray crystallography, as well as by spectroelectrochemistry and magnetic and EPR techniques. The three complexes differ by the bridging dicarboxylato group between two six-coordinate axially compressed high-spin d^4 Mn^{III} ions. The Mn–Mn sep-



aration is 8.736, 10.912, and 15.103 Å in LMn($\text{OOCCH}=\text{CHCOO}$)MnL (**1**), LMn($\text{OOC}\text{C}_6\text{H}_4\text{COO}$)MnL (**2**), and LMn($\text{OOC}\text{C}_6\text{H}_4\text{C}_6\text{H}_4\text{COO}$)MnL (**3**), respectively. The anodic oxidation of these complexes is irreversible and is similar to the monomeric MnL(OAc) analogue. Complex **3** exhibited the lowest oxidation potential with two overlapping oxidation peaks indicating a slightly different oxidation potential for the two Mn^{III} redox centres. By using temperature dependent magnetic susceptibility and variable temperature-variable field (VT VH) magnetisation measurements and high-frequency and -field EPR (HFEPR) spectroscopy, the single-ion spin Hamiltonian parameters (*g* values, ZFS parameters *D* and *E*) were obtained and reproduced successfully by *ab initio* calculations. The quality of HFEPR spectra of **1** and **2** was superior to that of the analogous mononuclear complex MnL(OAc). This allowed identification of characteristic signatures in high-resolution spectra which presumably indicate very weak exchange interactions between the paramagnetic ions and estimation of the exchange coupling constant, $|J| \approx 0.03(5) \text{ cm}^{-1}$, (J_1S_2 formalism) which was in reasonable agreement with DFT calculations for **1** and **2**. This result suggests that magnetic exchange interactions can occur in di-Mn^{III} systems over relatively long distances (as much as ~11 Å), which may be the case in biological di- and multi-Mn systems as well.

Conflicts of interest

The authors declare no competing interest.

Acknowledgements

This work was supported by a grant of Romanian Ministry of Research and Innovation, CNCS – UEFISCDI, project number PN-III-P4-ID-PCE-2016-0642, within PNCDI III (Contract 114/2017). The financial support of the Austrian Agency for International Cooperation in Education and Research (OEAD) (grant no. SK01/2018). This work was supported by the Science and Technology Assistance Agency under the contract no. APVV-15-0053 and APVV-15-0079 and SK-AT-2017-0017, by the Slovak Grant Agency VEGA under contract no. 1/0598/16, 1/0416/17 and 1/0466/18 and by the Ministry of Education, Science, Research and Sport of the Slovak Republic for funding within the scheme “Excellent research teams”. We thank the HPC centre at the Slovak University of Technology in Bratislava, which is a part of the Slovak Infrastructure of High Performance Computing (SIVVP Project, ITMS code 26230120002, funded by the European Region Development Funds), for computing facilities. A portion of this work was performed at the National High Magnetic Field Laboratory, which is supported by National Science Foundation Cooperative Agreements No. DMR-1157490 and DMR-1644779 and the State of Florida. This work was also supported by the Ministerio Español de Ciencia e Innovación (Projects

CTQ2016-75068P and CTQ2016-75671P and Unidad de Excelencia María de Maetzu MDM-2015-0538).

References

- 1 A. J. Wu, J. E. Penner-Hahn and V. L. Pecoraro, *Chem. Rev.*, 2004, **104**, 903–938.
- 2 V. V. Barynin, M. M. Whittaker, S. V. Antonyuk, V. S. Lamzin, P. M. Harrison, P. J. Artymiuk and J. W. Whittaker, *Structure*, 2001, **9**, 725–738.
- 3 S. V. Antonyuk, V. R. Melik-Adamyan, A. N. Popov, V. S. Lamzin, P. D. Hempstead, P. M. Harrison, P. J. Artymiuk and V. V. Barynin, *Crystallogr. Rep.*, 2000, **45**, 105–116.
- 4 J. A. Cotruvo and J. Stubbe, *Biochemistry*, 2010, **49**, 1297–1309.
- 5 N. Cox, H. Ogata, P. Stolle, E. Reijerse, G. Auling and W. Lubitz, *J. Am. Chem. Soc.*, 2010, **132**, 11197–11213.
- 6 (a) L. R. Scolnick, Z. F. Kanyo, R. C. Cavalli, D. E. Ash and D. W. Christianson, *Biochemistry*, 1997, **36**, 10558–10565; (b) Y. Hai and D. W. Christianson, *Acta Crystallogr., Sect. F: Struct. Biol. Commun.*, 2016, **72**, 300–306.
- 7 R. Cammack, A. Chapman, W.-P. Lu, A. Karagouni and D. P. Kelly, *FEBS Lett.*, 1989, **253**, 239–243.
- 8 K. S. Pedersen, M. Sigris, H. Weihe, A. D. Bond, C. Aa. Thuesen, K. P. Simonsen, T. Birk, H. Mutka, A.-L. Barra and J. Bendix, *Inorg. Chem.*, 2014, **53**, 5013–5019.
- 9 D. Tétard, A. Rabion, J.-B. Verlhac and J. Guilhem, *J. Chem. Soc., Chem. Commun.*, 1995, 531–532.
- 10 M. Retegan, M.-N. Collomb, F. Neese and C. Duboc, *Phys. Chem. Chem. Phys.*, 2013, **15**, 223–234.
- 11 C. Bolm, N. Meyer, G. Raabe, T. Weyhermüller and E. Bothe, *Chem. Commun.*, 2000, 2435–2436.
- 12 (a) P. Mathur, M. Crowder and G. C. Dismukes, *J. Am. Chem. Soc.*, 1987, **109**, 5227–5233; (b) E. J. Larson and V. L. Pecoraro, *J. Am. Chem. Soc.*, 1991, **113**, 7809–7810; (c) A. Gelasco and V. L. Pecoraro, *J. Am. Chem. Soc.*, 1993, **115**, 7928–7929; (d) D. R. Gamelin, M. L. Kirk, T. L. Stemmler, S. Pal, W. H. Armstrong, J. E. Penner-Hahn and E. I. Solomon, *J. Am. Chem. Soc.*, 1994, **116**, 2392–2399.
- 13 I. Romero, L. Dubois, M.-N. Collomb, A. Deronzier, J.-M. Latour and J. Pécaut, *Inorg. Chem.*, 2002, **41**, 1795–1806.
- 14 (a) S. Ménage, J.-J. Girerd and A. Gleizes, *J. Chem. Soc., Chem. Commun.*, 1988, 431–433; (b) J. B. Vincent, H.-L. Tsai, A. G. Blackman, S. Wang, P. D. W. Boyd, K. Folting, J. C. Huffman, E. B. Lobkovsky, D. N. Hendrickson and G. Christou, *J. Am. Chem. Soc.*, 1993, **115**, 12353–12361; (c) P. J. Pessiki, S. V. Khangulov, D. M. Ho and G. C. Dismukes, *J. Am. Chem. Soc.*, 1994, **116**, 891–897; (d) L. Dubois, D.-F. Xiang, X.-S. Tan, J. Pécaut, P. Jones, S. Baudron, L. Le Pape, J.-M. Latour, C. Baffert, S. Chardon-Noblat, M.-N. Collomb and A. Deronzier, *Inorg. Chem.*, 2003, **42**, 750–760.





15 L. Escriche-Tur, M. Corbella, M. Font-Bardia, I. Castro, L. Bonneviot and B. Albela, *Inorg. Chem.*, 2015, **54**, 10111–10125.

16 C. Palopoli, N. Bruzzo, C. Hureau, S. Ladeira, D. Murgida and S. Signorella, *Inorg. Chem.*, 2011, **50**, 8973–8983.

17 V. Solís, C. Palopoli, V. Daier, E. Rivièvre, F. Collin, D. M. Moreno, C. Hureau and S. Signorella, *J. Inorg. Biochem.*, 2018, **182**, 29–36.

18 S. Signorella, C. Palopoli and G. Ledesma, *Coord. Chem. Rev.*, 2018, **365**, 75–102.

19 (a) D. Moreno, C. Palopoli, V. Daier, S. Shova, L. Vendier, M. González Sierra, J.-P. Tuchagues and S. Signorella, *Dalton Trans.*, 2006, 5156–5166; (b) V. Daier, H. Biava, C. Palopoli, S. Shova, J.-P. Tuchagues and S. Signorella, *J. Inorg. Biochem.*, 2004, **98**, 1806–1817; (c) H. Blava, C. Palopoli, C. Duhayon, J.-P. Tuchagues and S. Signorella, *Inorg. Chem.*, 2009, **48**, 3205–3214; (d) H. Biava, C. Palopoli, S. Shova, M. De Gaudio, V. Daier, M. González-Sierra, J.-P. Tuchagues and S. Signorella, *J. Inorg. Biochem.*, 2006, **100**, 1660–1671.

20 L. A. Berben and J. C. Peters, *Inorg. Chem.*, 2008, **47**, 11669–11679.

21 F.-J. Wu, D. M. Kurtz Jr., K. S. Hagen, P. D. Nyman, P. G. Debrunner and V. A. Vankai, *Inorg. Chem.*, 1990, **29**, 5174–5183.

22 D. V. Wright, H. J. Mok, C. E. Dubé and W. H. Armstrong, *Inorg. Chem.*, 1998, **37**, 3714–3718.

23 (a) K. Wieghardt, U. Bossek, D. Ventur and J. Weiss, *J. Chem. Soc., Chem. Commun.*, 1985, 347–349; (b) K. Wieghardt, U. Bossek, B. Nuber, J. Weiss, J. Bonvoisin, M. Corbella, S. E. Vitols and J. J. Girerd, *J. Am. Chem. Soc.*, 1988, **110**, 7398–7411; (c) U. Bossek, K. Wieghardt, B. Nuber and J. Weiss, *Inorg. Chim. Acta*, 1989, **165**, 123–129.

24 T. C. Brunold, D. R. Gamelin and E. I. Solomon, *J. Am. Chem. Soc.*, 2000, **122**, 8511–8523.

25 J. E. Sheats, R. S. Czernuszewicz, G. C. Dismukes, A. L. Reingold, V. Petrouleas, J. Stubbe, W. H. Armstrong, R. H. Beer and S. J. Lippard, *J. Am. Chem. Soc.*, 1987, **109**, 1435–1444.

26 M. Hirotsu, N. Ohno, T. Nakajima, C. Kushibe, K. Ueno and I. Kinoshita, *Dalton Trans.*, 2010, **39**, 139–148.

27 G. Aromi, P. Gamez, O. Roubeau, P. C. Berzal, K. Kooijman, A. L. Spek, W. L. Driessens and J. Reedijk, *Inorg. Chem.*, 2002, **41**, 3673–3683.

28 J. Liu, J. Krzystek, S. Hill, L. Barrios and G. Aromi, *Inorg. Chem.*, 2013, **52**, 718–723.

29 N. N. Gerasimchuk, A. Gerges, T. Clifford, A. Danby and K. Bowman-James, *Inorg. Chem.*, 1999, **38**, 5633–5636.

30 S. J. Brudenell, L. Spiccia, A. M. Bond, G. D. Fallon, D. C. R. Hockless, G. Lazarev, P. J. Mahon and E. R. T. Tiekkink, *Inorg. Chem.*, 2000, **39**, 881–892.

31 A. Soroceanu, M. Cazacu, S. Shova, C. Turta, J. Kožíšek, M. Gall, M. Breza, P. Raptá, T. C. O. Mac Leod, A. J. L. Pombeiro, J. Telser, A. Dobrov and V. B. Arion, *Eur. J. Inorg. Chem.*, 2013, 1458–1474.

32 M. Cazacu, S. Shova, A. Soroceanu, P. Machata, L. Bucinsky, M. Breza, P. Raptá, J. Telser, J. Krzystek and V. B. Arion, *Inorg. Chem.*, 2015, **54**, 5691–5706.

33 S. Shova, M. Cazacu, G. Novitchi, G. Zoppellaro, C. Train and V. B. Arion, *Dalton Trans.*, 2017, **46**, 1789–1793.

34 S. Shova, A. Vlad, M. Cazacu, J. Krzystek, L. Bucinsky, M. Breza, D. Darvasiová, P. Raptá, J. Cano, J. Telser and V. B. Arion, *Dalton Trans.*, 2017, **46**, 11817–11829.

35 C. Teutloff, K.-O. Schäfer, S. Sinnecker, V. Barynin, R. Bittl, K. Wieghardt, F. Lendzian and W. Lubitz, *Magn. Reson. Chem.*, 2005, **43**, S51–S64.

36 K.-O. Schäfer, R. Bittl, F. Lendzian, V. Barynin, T. Weyhermüller, K. Wieghardt and W. Lubitz, *J. Phys. Chem. B*, 2003, **107**, 1242–1250.

37 L. Rapatskiy, W. M. Ames, M. Pérez-Navarro, A. Savitsky, J. J. Giese, T. Weyhermüller, H. S. Shafaat, M. Högbom, F. Neese, D. A. Pantazis and N. Cox, *J. Phys. Chem. B*, 2015, **119**, 13904–13921.

38 A. Constantatos, R. Bewley, A.-L. Barra, J. Bendix, S. Piligkos and H. Weihe, *Inorg. Chem.*, 2016, **55**, 10377–10382.

39 SAINT-Plus, v. 7.06a, Bruker-Nonius AXS Inc., Madison, WI, 2004; APEX2, Bruker-Nonius AXS Inc., Madison, WI, 2004.

40 O. V. Dolomanov, L. J. Bourhis, R. J. Gildea, J. A. K. Howard and H. Puschmann, *J. Appl. Crystallogr.*, 2009, **42**, 339–341.

41 G. M. Sheldrick, *Acta Crystallogr., Sect. A: Found. Crystallogr.*, 2008, **64**, 112–122.

42 J. Cano, *VPMAG Package*, University of València, Spain, 2003.

43 A. K. Hassan, L. A. Pardi, J. Krzystek, A. Sienkiewicz, P. Goy, M. Rohrer and L. C. Brunel, *J. Magn. Reson.*, 2000, **142**, 300–312.

44 F. Neese, *Wiley Interdiscip. Rev.: Comput. Mol. Sci.*, 2018, **8**, e1327.

45 (a) J. P. Perdew, K. Burke and M. Ernzerhof, *Phys. Rev. Lett.*, 1997, **78**, 1396; (b) J. P. Perdew, K. Burke and M. Ernzerhof, *Phys. Rev. Lett.*, 1996, **77**, 3865–3868.

46 A. Schäfer, C. Huber and R. Ahlrichs, *J. Chem. Phys.*, 1994, **100**, 5829–5835.

47 A. Schäfer, H. Horn and R. Ahlrichs, *J. Chem. Phys.*, 1992, **97**, 2571–2577.

48 A. Schäfer, C. Huber and R. Ahlrichs, *J. Chem. Phys.*, 1994, **100**, 5829–5835.

49 K. Eichkorn, O. Treutler, H. Ohm, M. Haser and R. Ahlrichs, *Chem. Phys. Lett.*, 1995, **240**, 283–290.

50 K. Eichkorn, O. Treutler, H. Ohm, M. Haser and R. Ahlrichs, *Chem. Phys. Lett.*, 1995, **242**, 652–660.

51 K. Eichkorn, O. Treutler, H. Ohm, M. Haser and R. Ahlrichs, *Theor. Chem. Acc.*, 1997, **97**, 119–124.

52 (a) C. Angeli, R. Cimiraglia, S. Evangelisti, T. Leininger and J.-P. Malrieu, *J. Chem. Phys.*, 2001, **114**, 10252; (b) C. G. Werncke, E. Suturina, P. C. Bunting, L. Vendier, J. R. Long, M. Atanasov, F. Neese, S. Sabo-Etienne and S. Bontemps, *Chem. – Eur. J.*, 2016, **22**(5), 1668–1674.

53 (a) A. D. Becke, *Phys. Rev. A*, 1988, **38**, 3098–3100; (b) C. Lee, W. Yang and R. G. Parr, *Phys. Rev. B: Condens. Matter Mater. Phys.*, 1988, **37**, 785–789.

54 (a) R. Krishnan, J. S. Binkley, R. Seeger and J. A. Pople, *J. Chem. Phys.*, 1980, **72**, 650–654; (b) A. D. McLean and G. S. Chandler, *J. Chem. Phys.*, 1980, **72**, 5639–5648.

55 (a) F. Neese, *J. Am. Chem. Soc.*, 2006, **128**, 10213–10222; (b) C. Duboc, D. Ganyushin, K. Sivalingam, M. N. Collomb and F. Neese, *J. Phys. Chem. A*, 2010, **114**, 10750–10758.

56 (a) M. Retegan, N. Cox, D. A. Pantazis and F. Neese, *Inorg. Chem.*, 2014, **53**, 11785–11793; (b) H. Fliegl, K. Fink, W. Klopper, C. E. Anson, A. K. Powell and R. Clerac, *Phys. Chem. Chem. Phys.*, 2009, **11**, 3900–3909.

57 M. J. Frisch, G. W. Trucks, H. B. Schlegel, G. E. Scuseria, M. A. Robb, J. R. Cheeseman, G. Scalmani, V. Barone, B. Mennucci, G. A. Petersson, H. Nakatsuji, M. Caricato, X. Li, H. P. Hratchian, A. F. Izmaylov, J. Bloino, G. Zheng, J. L. Sonnenberg, M. Hada, M. Ehara, K. Toyota, R. Fukuda, J. Hasegawa, M. Ishida, T. Nakajima, Y. Honda, O. Kitao, H. Nakai, T. Vreven, J. A. Montgomery, J. E. Peralta, F. Ogliaro, M. Bearpark, J. J. Heyd, E. Brothers, K. N. Kudin, V. N. Staroverov, R. Kobayashi, J. Normand, K. Raghavachari, A. Rendell, J. C. Burant, S. S. Iyengar, J. Tomasi, M. Cossi, N. Rega, J. M. Millam, M. Klene, J. E. Knox, J. B. Cross, V. Bakken, C. V. Adamo, J. Jaramillo, R. Gomperts, R. E. Stratmann, O. Yazyev, A. J. Austin, R. Cammi, C. Pomelli, J. W. Ochterski, R. L. Martin, K. Morokuma, V. G. Zakrzewski, G. A. Voth, P. Salvador, J. J. Dannenberg, S. Dapprich, A. D. Daniels, Ö. Farkas, J. B. Foresman, J. V. Ortiz, D. Cioslowski and D. J. Fox, Gaussian, Inc., Wallingford, CT, 2009.

58 R. Bauernschmitt and R. Ahlrichs, *Chem. Phys. Lett.*, 1996, **256**, 454–464.

59 P. Flükiger, H. P. Lüthi, S. Sortmann and J. Weber, MOLEKEL 4.3, Swiss Center for Scientific Computing, Manno, Switzerland, 2002.

60 A. D. Becke, *J. Chem. Phys.*, 1993, **98**, 5648–5652.

61 E. Ruiz, A. Rodríguez-Forteá, J. Cano, S. Alvarez and P. Alemany, *J. Comput. Chem.*, 2003, **24**, 982–989.

62 E. Ruiz, J. Cano, S. Alvarez and P. Alemany, *J. Comput. Chem.*, 1999, **20**, 1391–1400.

63 E. Ruiz, J. Cano, S. Alvarez and P. Alemany, *J. Am. Chem. Soc.*, 1998, **120**, 11122–11129.

64 J. Tomasi, B. Mennucci and E. Cancès, *J. Mol. Struct.: THEOCHEM*, 1999, **464**, 211–226.

65 M. K. Chan and W. H. Armstrong, *Inorg. Chem.*, 1989, **28**, 3777–3779.

66 V. C. Quee-Smith, L. DelPizzo, S. H. Jureller, J. L. Kerschner and R. Hage, *Inorg. Chem.*, 1996, **35**, 6461–6465.

67 M. Zlatar, M. Gruden, O. Yu. Vassillyeva, E. A. Buvaylo, A. N. Ponomarev, S. A. Zvyagin, J. Wosnitza, J. Krzystek, P. Garcia-Fernandez and C. Duboc, *Inorg. Chem.*, 2016, **55**, 1192–1201.

68 A. Ceulemans, L. F. Chibotaru, G. A. Heylen, K. Pierloot and L. G. Vanquickenborne, *Chem. Rev.*, 2000, **100**, 787–806.

69 (a) S. Romain, C. Duboc, F. Neese, E. Riviere, L. R. Hanton, A. G. Blackman, C. Philouze, J.-C. Lepretre, A. Deronzier and M.-N. Collomb, *Chem. – Eur. J.*, 2009, **15**, 980–988; (b) G. A. Craig, J. J. Marbey, S. Hill, O. Rubeau, S. Parsons and M. Murrie, *Inorg. Chem.*, 2015, **54**, 13–15; (c) J. Telser, J. Krzystek and A. Ozarowski, *J. Biol. Inorg. Chem.*, 2014, **19**, 297–318; (d) J. Krzystek and J. Telser, *Dalton Trans.*, 2016, **45**, 16751–16763; (e) J. Valejo, A. Pascual-Alvarez, J. Cano, I. Castro, M. Julve, F. Lloret, J. Krzystek, G. De Munno, D. Armentano, W. Wernsdorfer, R. Ruiz-Garcia and E. Pardo, *Angew. Chem., Int. Ed.*, 2013, **52**, 14075–14079; (f) Q. Scheifele, C. Riplinger, F. Neese, H. Weihe, A.-L. Barra, F. Juranyi, A. Podlesnyak and P. L. W. Tregenna-Piggott, *Inorg. Chem.*, 2008, **47**, 439–447; (g) C. Mantel, H. Chen, R. H. Crabtree, C. W. Brudwig, J. Pécaut, M.-N. Collomb and C. Duboc, *ChemPhysChem*, 2005, **6**, 541–546; (h) B. Albela, R. Carina, C. Policar, S. Poussereau, J. Cano, J. Guilhem, L. Tchertanov, G. Blondin, M. Delroisse and J.-J. Girerd, *Inorg. Chem.*, 2005, **44**, 6959–6966.

70 H. J. Gerritsen and E. S. Sabisky, *Phys. Rev.*, 1963, **132**, 1507–1512.

71 I. Krivokapic, C. Noble, S. Klitgaard, P. Tregenna-Piggott, H. Weihe and A.-L. Barra, *Angew. Chem., Int. Ed.*, 2005, **44**, 3613–3616.

72 J. Krzystek, S. A. Zvyagin, A. Ozarowski, S. Trofimenco and J. Telser, *J. Magn. Reson.*, 2006, **178**, 174–183.

73 F. T. de Oliveira, E. L. Bominaar, J. Hitst, J. A. Fee and E. Münck, *J. Am. Chem. Soc.*, 2004, **126**, 5338–5339.

74 The inversion symmetry of the complexes means that sources of anisotropic coupling other than magnetic dipole-dipole (e.g., Dzialoshinskii-Moriya)⁷³ can be disregarded.

75 N. Berg, T. Rajeshkumar, S. M. Taylor, E. K. Brechin, G. Rajaraman and L. F. Jones, *Chem. – Eur. J.*, 2012, **18**, 5906–5918.

76 T. J. Morsing, J. Bendix, H. Weihe and A. Dössing, *Inorg. Chem.*, 2014, **53**, 2996–3003.

77 (a) H. Weihe and H. U. Güdel, *J. Am. Chem. Soc.*, 1997, **119**, 6539–6543; (b) H. Weihe and H. U. Güdel, *J. Am. Chem. Soc.*, 1998, **120**, 2870–2879.

78 (a) O. V. Nesterova, D. S. Nesterov, J. Jezierska, A. J. L. Pombeiro and A. Ozarowski, *Inorg. Chem.*, 2018, **57**, 12384–12397; (b) A. Switlicka, B. Machura, M. Penkala, A. Bienko, D. C. Bienko, J. Titis, C. Rajnak, R. Boca, A. Ozarowski and M. Ozerov, *Inorg. Chem.*, 2018, **57**, 12740–12755.

79 G. David, F. Wennmohs, F. Neese and N. Ferré, *Inorg. Chem.*, 2018, **57**, 12769–12776.

